Supplement of Atmos. Meas. Tech., 11, 4345–4360, 2018
https://doi.org/10.5194/amt-11-4345-2018-supplement

Atmospheric Measurement Techniques
Open Access
EGU

Supplement of

Exploring femtosecond laser ablation in single-particle aerosol mass spectrometry

Ramakrishna Ramisetty et al.

Correspondence to: Claudia Mohr (claudia.mohr@aces.su.se)

The supplementary information contains information about laser-matter interaction at different time scales, the number of mass spectra measured in each experiment with different lasers for different particle types, the sources of the different particles types, the calculation of the laser beam diameters and power densities, and the supporting information for fs-laser spectral selection and reproducibility.

Time scales of light-matter interaction

The laser ablation and ionization mechanism depends on the pulse duration of the laser. Figure S1 (taken from Hamad et. al. (2016) (a) and Royon et al. (2011) (b)) shows the ablation mechanism for different pulse durations and time scales.

Nanosecond laser ablation: The target material surface absorbs the energy and heats up, then thermal vaporization and ablation takes place. In ultra-short laser pulse ablation mutli-photon ionization, coulomb explosion, thermal vapourization and then plasma formation take place. At ultra-short femtosecond laser interaction, two different ablation regimes are observed: 1) non thermal Coulomb explosion upon multiphoton surface ionization is the dominant process, yielding electrons and fast ions. 2) At higher laser intensities, ablation exhibits signs of hyper-thermal emission (phase explosion) as a result of rapid hot electron thermalization. The fs-laser ablation makes more atomic ions than the nanosecond laser ablation due to rapid energy transfer, but also makes more ion clusters because of the explosion procesess. Hence, fs-laser ablation generates larger ion clusters than ns-laser ablation (Bulgakov et al., 2004; Harilal et al., 2014; Kato et al., 2007; Royon et al., 2011).

These procesess are explained and oberserved well for fixed target-laser interactions, however, they are rarely studied for air-borne particles (Murphy and Thomson, 1995; Zawadowicz et al., 2015; Zhou et al., 2007). Nevertheless, the physical mechanisms of the particle-laser interactions may be comparable especially for larger aerosol particles.

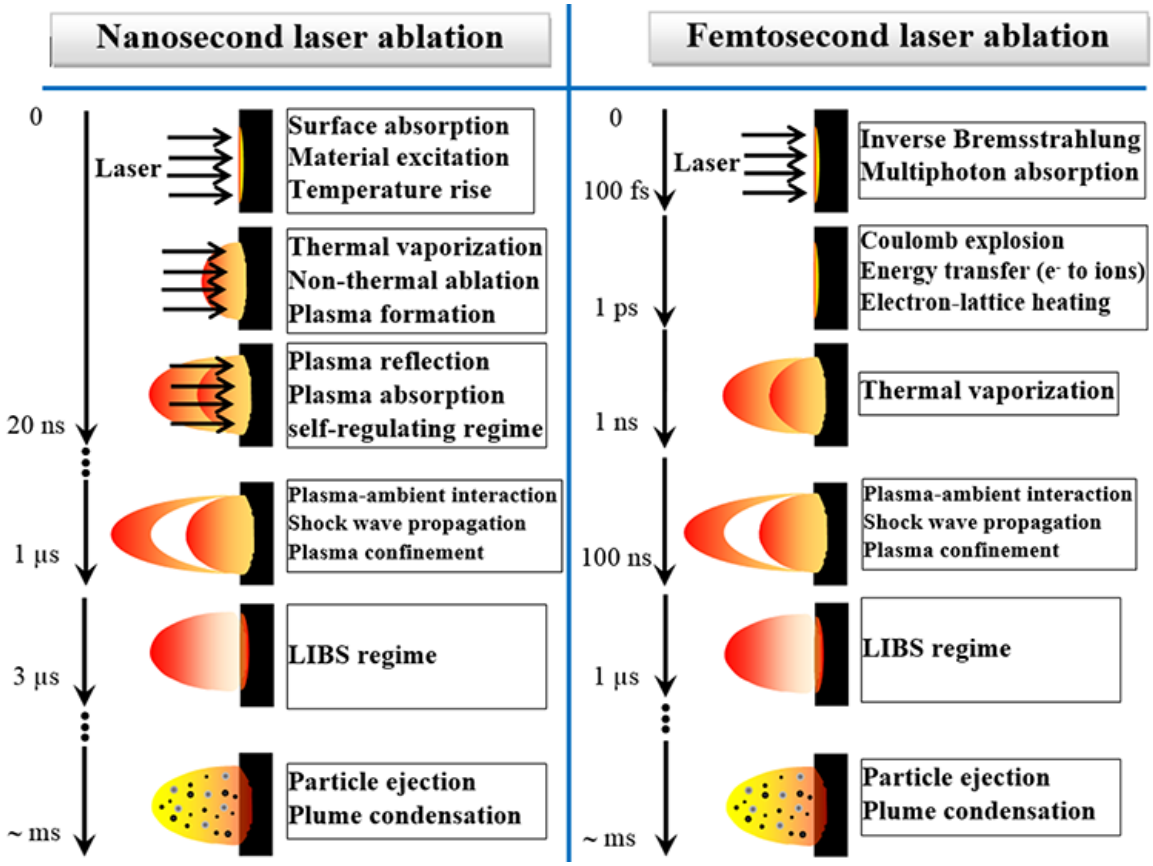

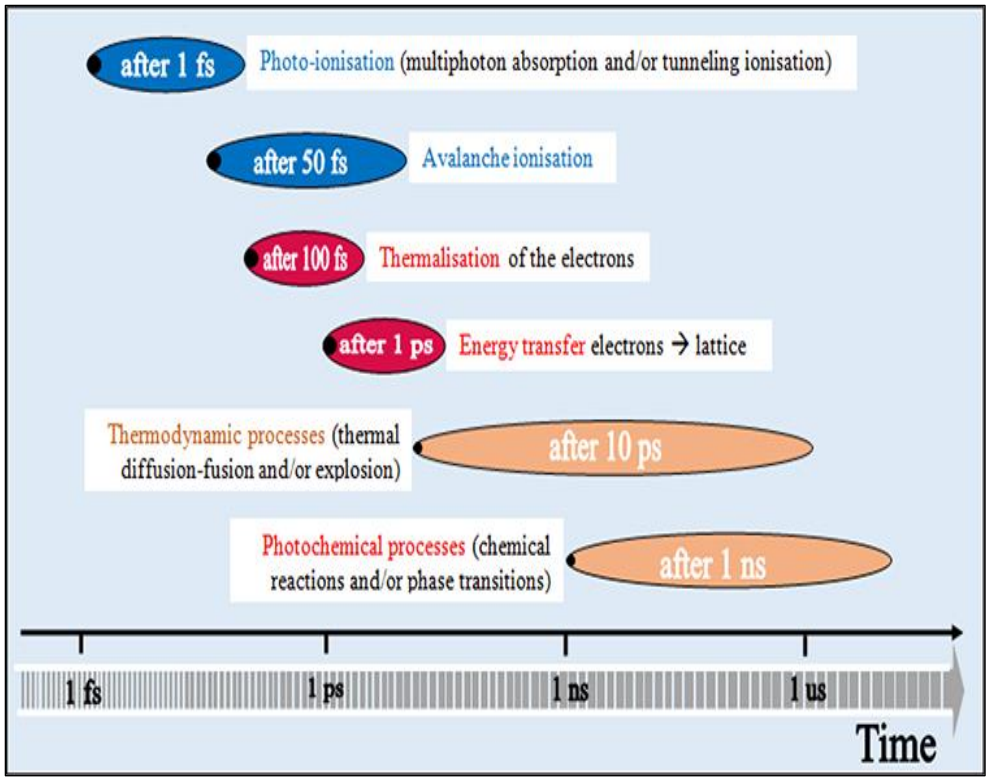

Figure S 1: (Top) Approximate time scales of nanosecond and femtosecond energy absorption and laser ablation along with various processes happening during and after the laser pulse is applied. (Bottom) Timescale of the physical phenomena involved in light-matter interaction.

Table S 1: Number of particles measured with ns-LAAPTOF with different pulse energies at focus positions F1 and F2. Typically more than 80 % of the spectra out of these are usable (non-empty spectra).

Particle types	Diameter *(d_p) nm*	Number of spectra obtained for three different laser energies					
		0.8 mJ		4 mJ		8 mJ	
		at F1	at F2	at F1	at F2	at F1	at F2
PSL500	500	420	500	437	500	452	500
PSL800	800	500	500	500	500	500	500
PSL1000	1000	500	500	500	500	500	500
Silica	1100	1000	1000	1000	1000	1000	1000
NaCl	400	443	1000	1000	1000	1000	1000
NH_4NO_3	400	500	500	500	500	500	500
Au-Ag	600	1000	1000	1000	1000	1000	1000
Au-SiO_2	400	1000	1000	1000	1000	1000	1000
Au-PAH	400	500	1000	500	1000	500	1000

35

Table S 2: Number of particles measured with fs-LAAPTOF with different pulse energies at focus positions F1 and F2. Typically, more than 40 % to 60 % of the spectra out of these are usable for the wavelength of 800 nm and less than 20 % are usable for 266 nm.

Particle types	Number of spectra obtained at 266 nm		Number of spectra obtained at 800 nm for four different laser energies							
	0.2 mJ		0.3 mJ		1.7 mJ		3.2 mJ		3.5 mJ	
	at F1	at F2	at F1	at F2	at F1	at F2	at F1	at F2	at F1	at F2
PSL500	500	750	10	50	500	500	1000	260	160	320
PSL800	500	NA	10	30	1000	200	1000	600	120	500
PSL1000	500	NA	10	20	300	500	130	310	1500	310
Silica	1000	450	300	120	1000	270	1000	430	1000	560
NaCl	1000	500	1000	1000	1000	1000	80	1000	500	400
NH_4NO_3	600	1000	60	50	500	380	1000	350	500	500
Au-Ag	1300	1000	140	10	1000	500	1500	500	500	250
Au-Silica	600	300	1000	10	500	200	650	580	350	240
Au-PAH	300	1000	20	10	1000	500	500	500	400	600

40

Table S 3: Particle samples used in this study. The samples marked by an asterisk were originally polydisperse, and size-selected through a DMA. d_m = electrical mobility diameter; d_p= geometric diameter.

Sample	Vendor	Particle diameter d_p (nm)
PSL500	Thermo Scientific®, USA	500
PSL800	Thermo Scientific®, USA	800
PSL1000	Thermo Scientific®, USA	1000
NaCl	Merck KGaA	400
NH_4NO_3	Merck KGaA	400
SiO_2	Palas AG	1000
Au-Ag	Nanopartz Inc, USA	600 (300 nm core and 150 nm thick shell)
Au-PAH	Nanopartz Inc, USA	400 (300 nm core and 50 nm thick shell)
Au-SiO_2	Nanopartz Inc, USA	400 (300 nm core and 50 nm thick shell)

Beam diameter and power density calculations

The laser beam diameter at focus position is calculated by using the Equation 1 and for other positions calculated by Equation 2. (Graf, 2015)

Diameter at focus point = $d_f = \frac{d_e \times f}{\sqrt{{Z_{Re}}^2 + (Z_e - f)^2}}$ Eq. (1)

Where d_e = initial beam diameter

f = focal length

Z_{Re} = Raleigh length before the lens

Z_e = total distance from source to lens

Diameter at distance z from focus point = $d(z) = d_f \sqrt{1 + \frac{z^2}{{z_R}^2}}$ Eq. (2)

Spot size variation due to Spherical aberration= kD^3/f^2 Eq. (3)

k = function of refractive index of the lens

D = diameter of the beam at focus

f = focal length

The power densities acting on the particles were calculated using the beam diameters from table S4 and the following equation:

Power density = $\frac{energy\ per\ pulse}{pulse\ duration \times beam\ spot\ area}$ Eq. (4)

Table S 4: The laser beam diameters for different positions.

Laser Wavelength	Beam Diameter at Position F_2 (µm)	Beam Diameter at Position F_1 (µm)	Beam Diameter at Focus Position (µm)
fs-laser 800 nm	*246±36*	*487±77*	*42±9*
fs-laser 266 nm	*182±32*	*270±32*	*38±9*
ns-laser 193 nm	*81 ±7*	*99±31*	*37±2*

70

Variability of the total ion intensity for constant conditions collecting 500 mass spectra

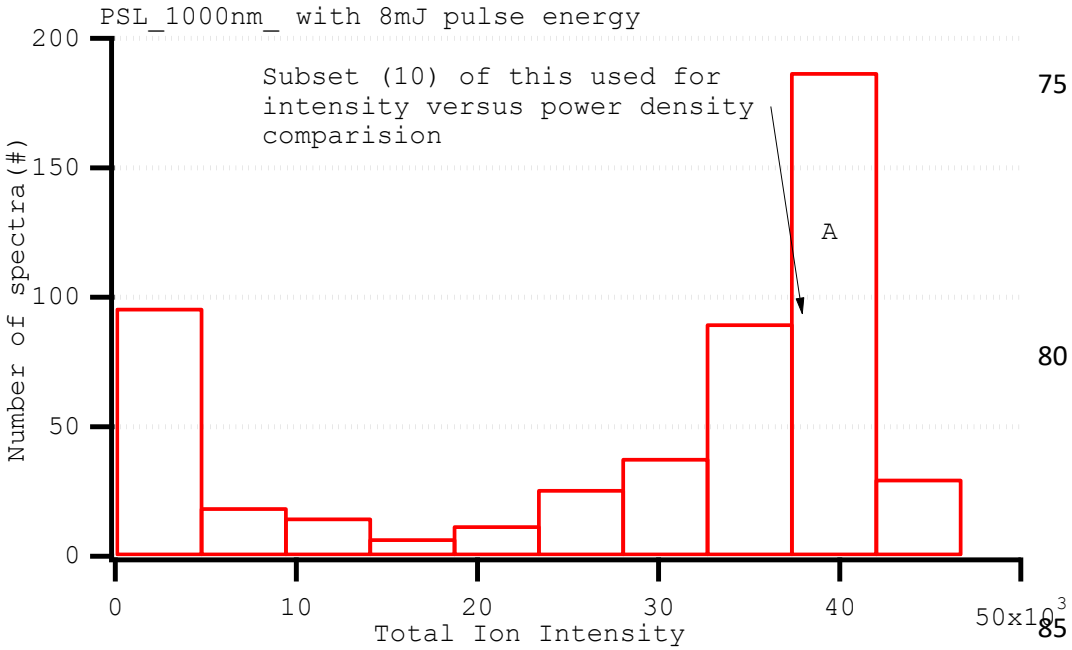

Figure S 2: Distribution of the number of spectra obtained for 1000 nm PSL particles with the ns-laser at 8 mJ energy for different total ion (both positive and negative) intensity. The 10 spectra were selected from section A shown in the plot. The Pearson's correlation coefficient is between 0.7 and 0.9 for these selected spectra.

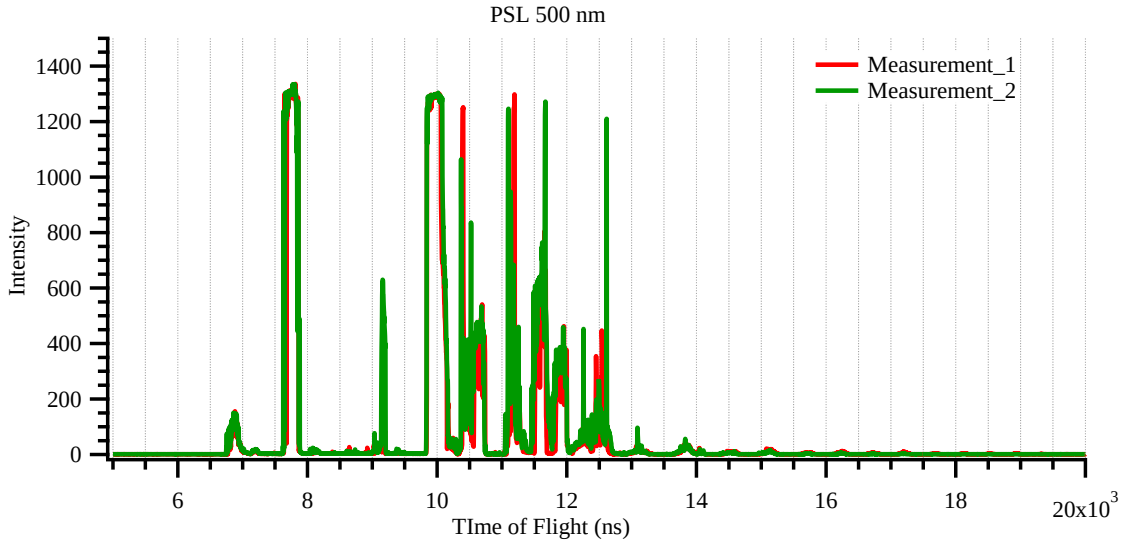

Figure S 3: Reproducibility of spectra observed with fs-laser for 500 nm PSL particles in two different measurements with same laser conditions (3.2 mJ, 800 nm and same focus position), the measurement_1 (red) and the measurement_2 (green) are the raw time-of-flight spectra, these are the average spectra of 500 particles. The spectral features are nearly same in different measurements, Pearson's correlation coefficient between these spectra is ~0.92, and the remaining relatively small shift in the peaks is due to the difference in initial ion timings.

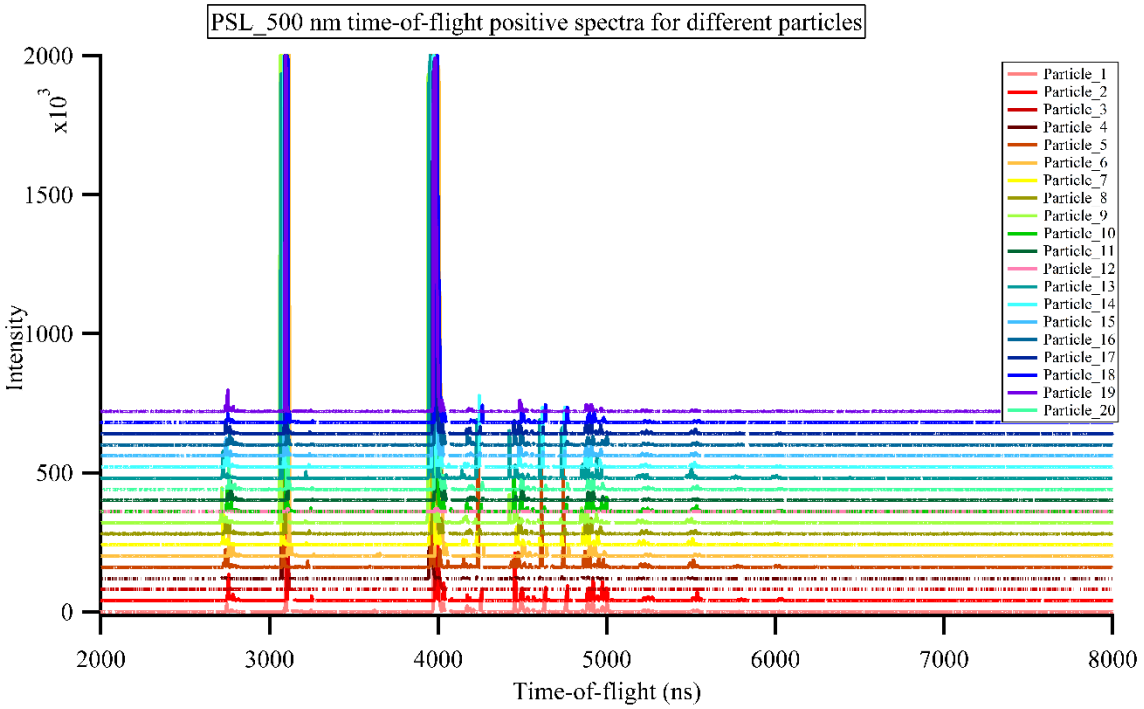

Figure S 4: Reproducibility of positive spectra observed with fs-laser ablation for 20 different single 500 nm PSL particles with 3.2 mJ energy per pulse. An off-set was added to the intensity scale to allow for better comparison. Pearson's correlation coefficient between these spectra is ~0.6-0.9 for these spectra.

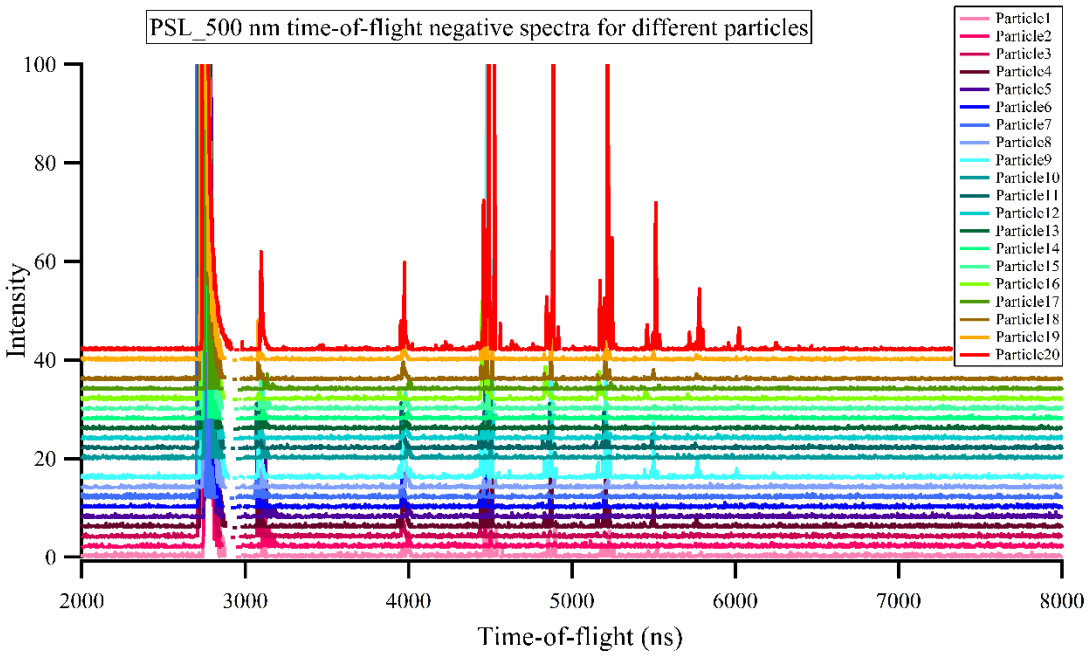

Figure S 5: Reproducibility of negative mass spectra observed with fs-laser ablation for 20 different single 500 nm PSL particles with 3.2 mJ energy per pulse. An off-set was added to the intensity scale to allow for better comparison. Pearson's correlation coefficient between these spectra is ~0.6-0.9 for these spectra.

SiO_2 mass spectra

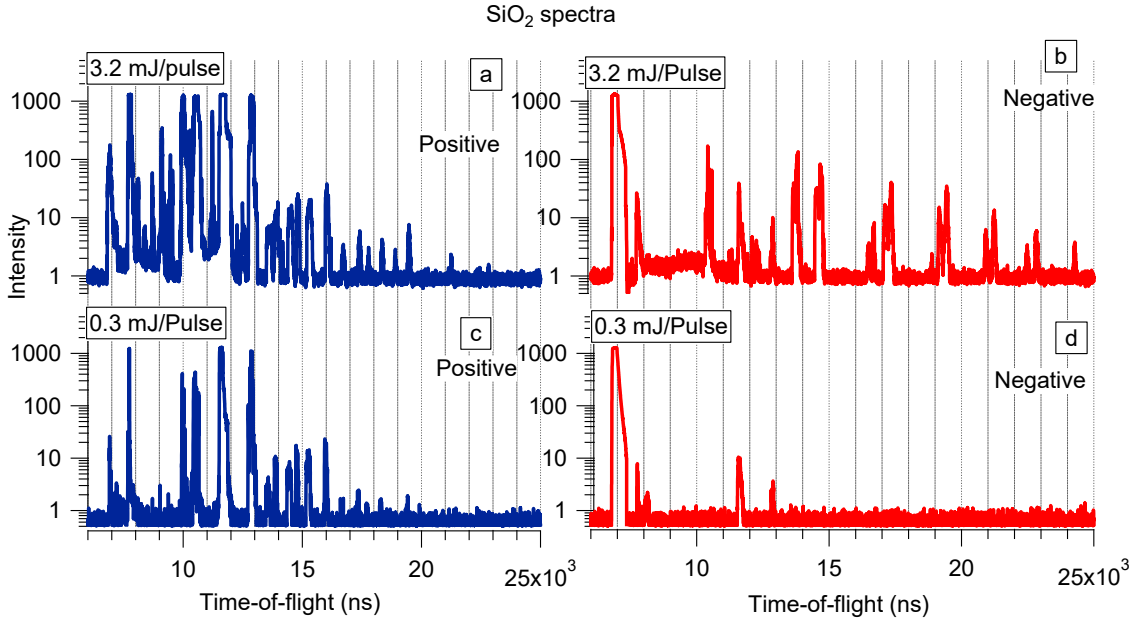

Figure S 6: SiO_2 raw spectra for different laser energies for fs-laser ablation at 800 nm. (a) & (b) are positive and negative spectra at 3.2 mJ energy per pulse (c) & (d) are positive and negative spectra at 0.3 mJ energy per pulse. More clusters form at higher pulse energies.

Comparison of single particle mass spectra obtained using 193 nm (ns pules), 266 nm (fs pulses), and 800 nm (fs pulses)

The mass spectra for PSL particles of 500 nm diameter are shown in Fig. S7c and Fig. S7d with the only remarkable difference being the reduced average ion intensity for 266 nm. These spectra are similar to the type-2 spectra (cf. Fig. 3e-f) obtained using the fs-laser with 800 nm. The ATOFMS with 266 nm nanosecond laser pulses generates similar positive ion spectra (Gälli et al., 2001) but more spectral signatures on the negative ion spectra.

For NaCl aerosol particles (cf. Fig. S8c-d), the 266 nm fs-LAAPTOF results in the same positive and negative spectra as for 800 nm (cf. Fig. 4c), and the major differences observed are less NaO_2^+ ions and less Cl^- peaks in the negative spectra for 266 nm. Na_2Cl^+, $NaCl_2^+$ also exist in the positive spectrum. Carson et al. (1997, 1995) generated very similar single particle mass spectra for NaCl particles with 248 nm, 5 mJ pulse energy, and 2.5 ns pulse duration. However, the average ion intensity is 4 times smaller than with 800 nm fs-laser pulses.

Ammonium nitrate particles (cf. Fig. S9c-d) ionized with 266 nm fs pulses result in the same positive (NO_2^{2+}, NO^+, and NO_2^+) ion spectral features as when using 800 nm fs pulses (cf. Fig. S9e-f), but with no NH_2^+/O^+, OH^+, NH_4^+ signature and less average ion intensity and more negative ion signatures. Brands et al. (2011) observed major peaks for $NO^{+/-}$, $NO_2^{+/-}$, N_2^+, NO_3^-, and more positive clusters with 266 nm ns pulses using an ATOFMS.

Single particle mass spectra for SiO_2 particles are shown in Fig. S10 for different desorption and ionization wavelengths. The mass spectra show very similar spectral features in the negative ion spectra for both 800 nm and 266 nm of the fs-laser, however, a smaller number of $Si_xO_y^+$ clusters is observed in the fs-laser 266 nm positive spectra. For 266 nm the intensities are smaller and hence the larger ions less visible. Furthermore, the O_2^+ ions are missing. Similar mass spectra were observed when using a 266 nm ATOFMS for Silicon rich particles with mainly SiO^- and SiO_2^- signatures (Dall´Osto et al., 2004).

For all core-shell particles (cf. Figs S11-S13), the spectral signatures originating from additional surface coatings e.g. by water or the surfactant (Cetyl-trimethylammonium bromide) are very similar when using fs-laser pulses of 266 and 800 nm. No gold signatures were observed for any of the core-shell particles using 266 nm and 800 nm fs-laser pulses, despite the lower reflectivity of gold in the UV. Spencer et al. (2008) have observed surface plasmon effects with 266 nm nanosecond ATOFMS during laser desorption and ionisation for gold nanoparticles. They reported very similar gold ion signatures as we have observed for 193 nm ns-laser pulses and silver coated gold particles. However, we could not detect any such gold related ion signatures with the fs-laser at 266 nm or 800 nm.

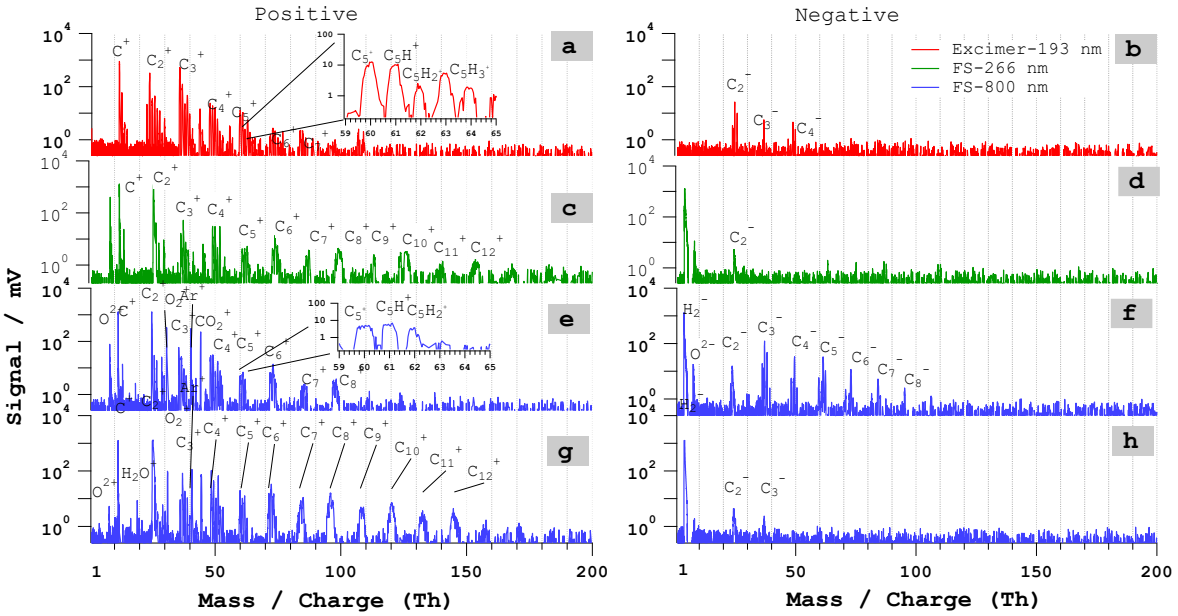

Figure S 7: Bipolar mass spectra of single PSL particles of dp= 500 nm. a – b: Typical ns-laser spectra (193 nm); c – d: fs-laser (λ = 266 nm) spectra; e-f: fs-laser (λ = 800 nm) spectra for 54 % of particles (type 1); g –h: fs-laser (λ = 800 nm) spectra for 42 % of particles (type 2). The pulse energy is 4 mJ for the ns-laser, 0.2 mJ for fs-266 nm, and 3.2 mJ for the fs-800 nm.

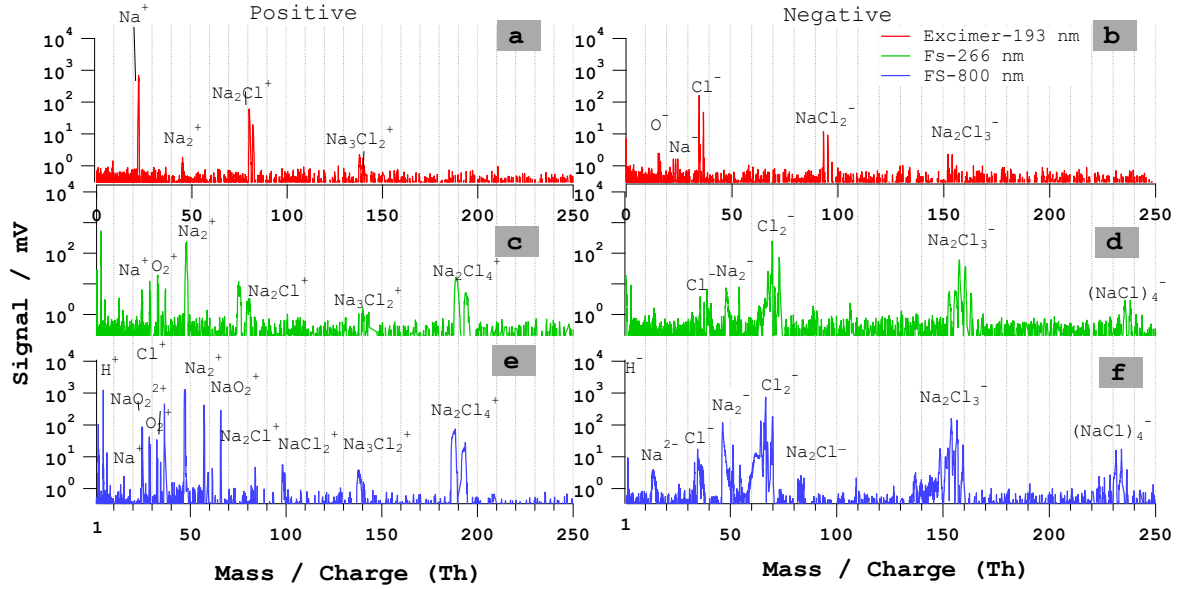

Figure S 8: Bipolar mass spectra of NaCl single particles of dm= 400 nm. a – b: Typical ns-laser spectra (193 nm); c – d: fs-laser (λ = 266 nm) spectra. e – f: fs-laser (λ = 800 nm) spectra. The pulse energy is 4 mJ for the ns-laser, 0.2 mJ for fs-266 nm, and 3.2 mJ for the fs-800 nm.

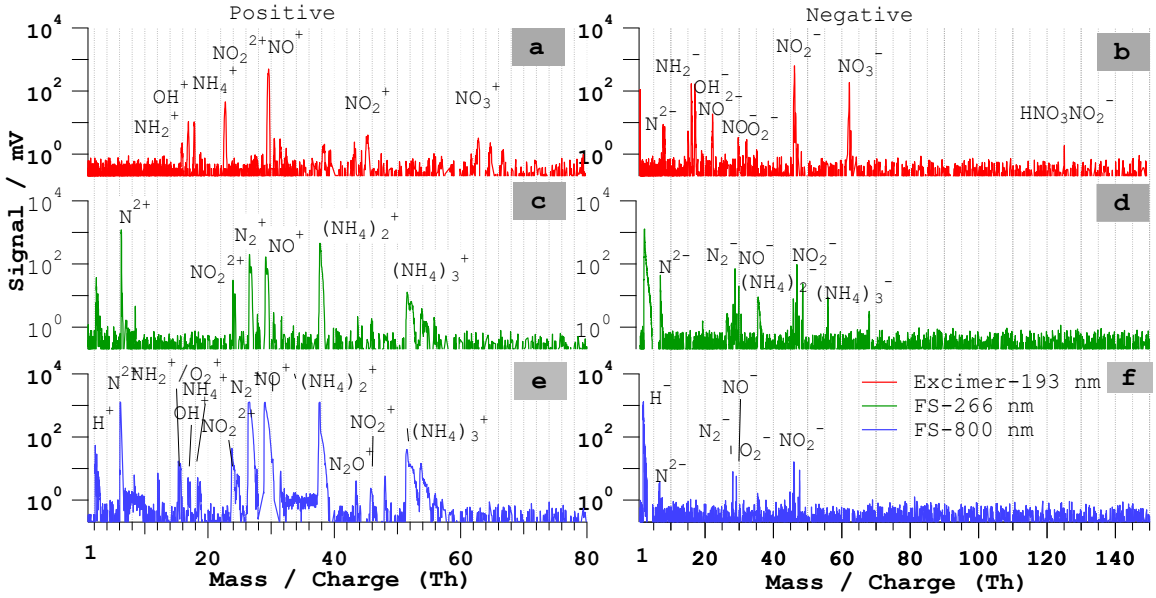

Figure S 9: Bipolar mass spectra of NH_4NO_3 particles of d_p= 400 nm. a – b: Typical ns-LAAPTOF spectra (193 nm); c – d: fs-LAAPTOF (λ = 266 nm) spectra. e – f: fs-laser (λ = 800 nm) spectra. The pulse energy is 4 mJ for the ns-laser, 0.2 mJ for fs-266 nm, and 3.2 mJ for the fs-800 nm.

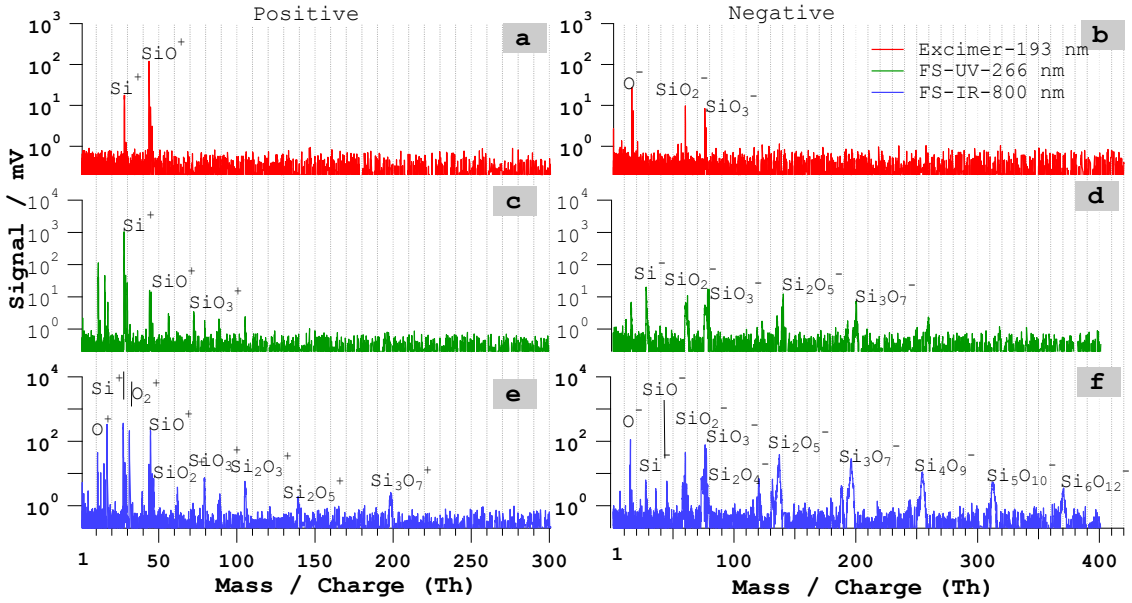

Figure S 10: Bipolar mass spectra of single SiO_2 particles of d_p= 500 nm. a – b: Typical ns-laser spectra (193 nm); c – d: fs-laser (λ = 266 nm) spectra; e-f: fs-laser (λ = 800 nm) spectra. The pulse energy is 4 mJ for the ns-laser, 0.2 mJ for fs-266 nm, and 3.2 mJ for the fs-800 nm.

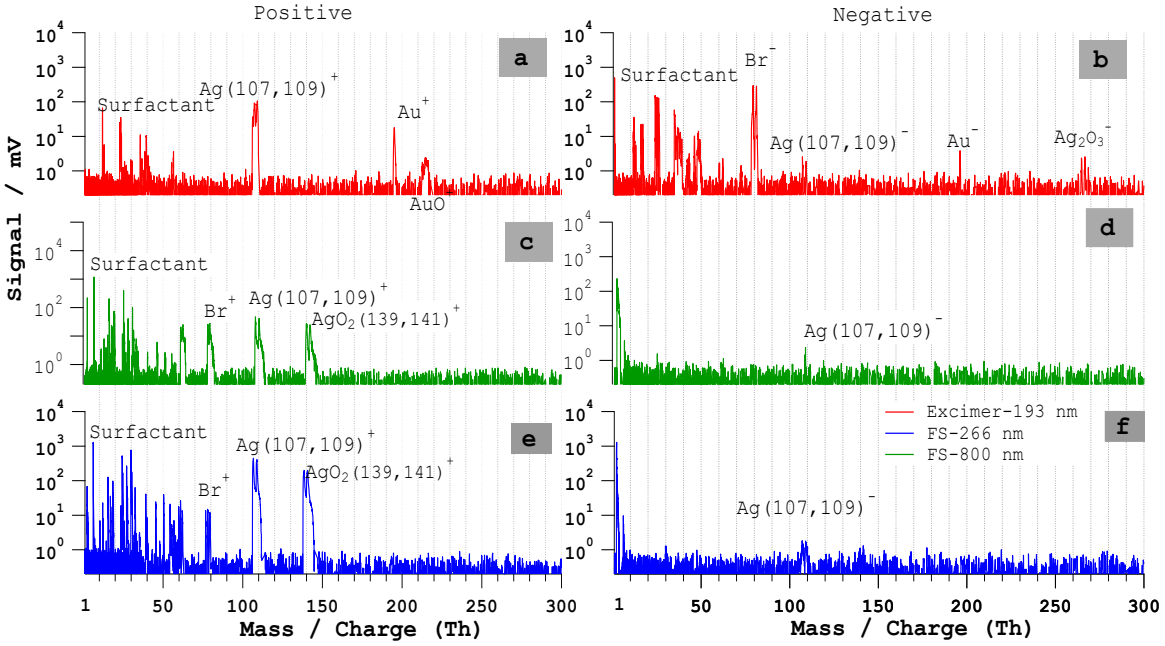

Figure S 11: Bipolar mass spectra of gold-silver core-shell particles of dp= 600 nm. a – b: Typical ns-LAAPTOF spectra (193 nm); c – d: fs-LAAPTOF (λ = 266 nm) spectra. e - f: fs-laser (λ = 800 nm) spectra. The pulse energy is 4 mJ for the ns-laser, 0.2 mJ for fs-266 nm, and 3.2 mJ for the fs-800 nm.

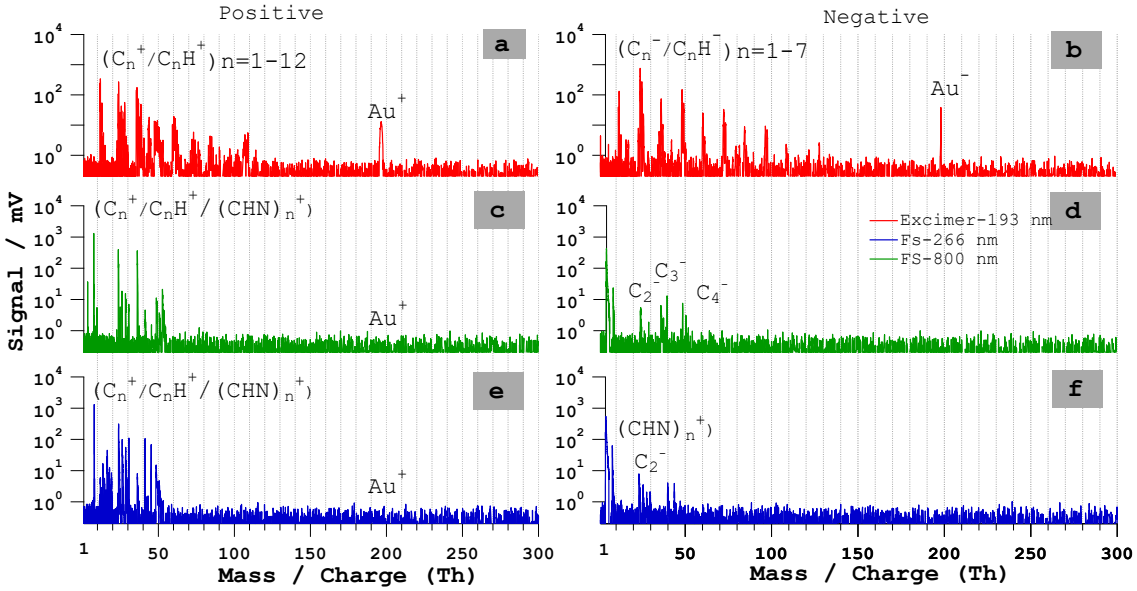

Figure S 12: Bipolar mass spectra of Au-PAH core-shell particles. a – b: Typical ns-LAAPTOF spectra (193 nm); c – d: fs-LAAPTOF (λ = 266 nm) spectrum that contains only PAH signal, e-f: fs-LAAPTOF (λ=800nm) spectrum also without gold signal. The pulse energy is 4 mJ for the ns-laser, 0.2 mJ for fs-266 nm, and 3.2 mJ for the fs-800 nm.

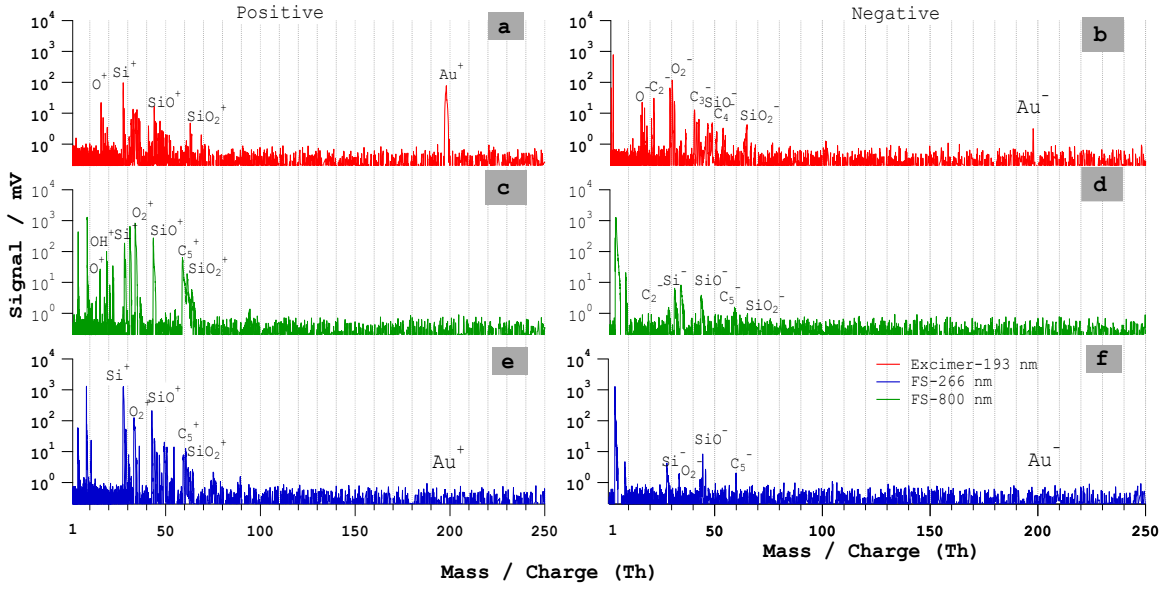

Figure S 13: Bipolar mass spectra of $AuSiO_2$ core-shell particles. a – b: Typical ns-LAAPTOF spectra (193 nm); c – d: fs-LAAPTOF (λ = 266 nm) spectrum that contains only SiO_2 signal, e-f: fs-LAAPTOF (λ=800nm) spectrum without gold signal. The pulse energy is 4 mJ for the ns-laser, 0.2 mJ for fs-266 nm, and 3.2 mJ for the fs-800 nm.

Variation of total average ion intensity with variation in the power density

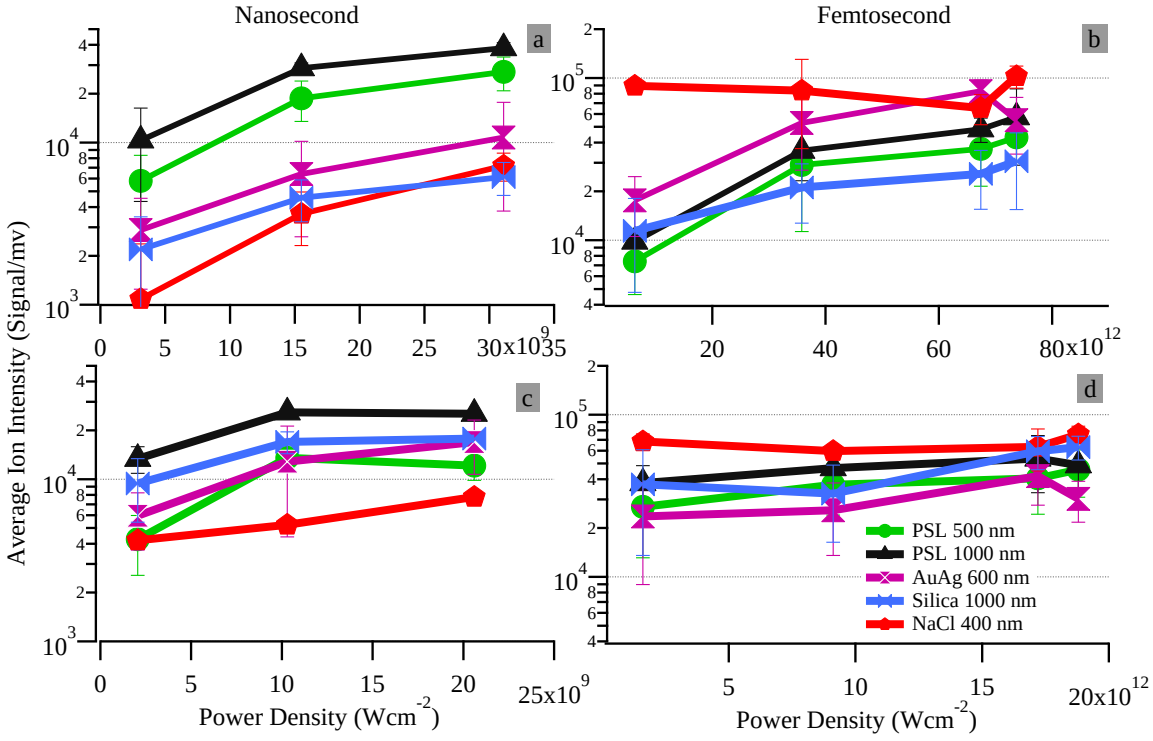

Figure S 14: Variation of average ion intensity for F1 and F2 position versus laser power density for different particle types. (a) – (b) Excimer laser, and (c) – (d) fs-laser, respectively. The power density of

the laser acting on the particles depends on the position of the focus relative to the particles, and it will be higher (by a factor of ~ 1.5) closer to focus postion (F2) than further away from the focus (F1). This corresponds to a difference of a factor of 2 for the average ion intensities. Error bars denote ± standard deviation.

References

Hamad, A. H.: High Energy and Short Pulse Lasers: Effects of Different Laser Pulse Regimes (Nanosecond, Picosecond and Femtosecond) on the Ablation of Materials for Production of Nanoparticles in Liquid Solution, 2016.

Royon, A., Petit, Y., Papon, G., Richardson, M., and Canioni, L.: Femtosecond laser induced photochemistry in materials tailored with photosensitive agents [Invited], Opt. Mater. Express, 1, 866-882, 2011.

Bulgakov, A. V., Ozerov, I., and Marine, W.: Silicon clusters produced by femtosecond laser ablation: non-thermal emission and gas-phase condensation, Applied Physics A, 79, 1591-1594, 2004.
Graf, T.: Laser - Grundlagen der Laserstrahlerzeugung. Springer Vieweg, 2015.

Harilal, S. S., Freeman, J. R., Diwakar, P. K., and Hassanein, A.: Femtosecond Laser Ablation: Fundamentals and Applications. In: Laser-Induced Breakdown Spectroscopy: Theory and Applications, Musazzi, S. and Perini, U. (Eds.), Springer Berlin Heidelberg, Berlin, Heidelberg, 2014.

Kato, T., Kobayashi, T., Matsuo, Y., Kurata-Nishimura, M., Oyama, R., Matsumura, Y., Yamamoto, H., Kawai, J., and Hayashizaki, Y.: Comparison between femtosecond and nanosecond laser ablation of solution samples applied on a substrate, Journal of Physics: Conference Series, 59, 372, 2007.

Murphy, D. M. and Thomson, D. S.: Laser Ionization Mass Spectroscopy of Single Aerosol Particles, Aerosol Science and Technology, 22, 237-249, 1995.

Royon, A., Petit, Y., Papon, G., Richardson, M., and Canioni, L.: Femtosecond laser induced photochemistry in materials tailored with photosensitive agents [Invited], Opt. Mater. Express, 1, 866-882, 2011.

Zawadowicz, M. A., Abdelmonem, A., Mohr, C., Saathoff, H., Froyd, K. D., Murphy, D. M., Leisner, T., and Cziczo, D. J.: Single-Particle Time-of-Flight Mass Spectrometry Utilizing a Femtosecond Desorption and Ionization Laser, Analytical Chemistry, 87, 12221-12229, 2015.

Zhou, L., Park, K., Milchberg, H. M., and Zachariah, M. R.: Understanding the Interaction of an Intense Laser Pulse with Nanoparticles: Application to the Quantification of Single Particle Mass Spectrometry, Aerosol Science and Technology, 41, 818-827, 2007.

Gälli, M., Guazzotti, S. A., and Prather, K. A.: Improved Lower Particle Size Limit for Aerosol Time-of-Flight Mass Spectrometry, Aerosol Science and Technology, 34, 381-385, 2001.

Carson, P. G., Johnston, M. V., and Wexler, A. S.: Real-Time Monitoring of the Surface and Total Composition of Aerosol Particles, Aerosol Science and Technology, 26, 291-300, 1997.

Carson, P. G., Neubauer, K. R., Johnston, M. V., and Wexler, A. S.: On-line chemical analysis of aerosols by rapid single-particle mass spectrometry, Journal of Aerosol Science, 26, 535-545, 1995.

Brands, M., Kamphus, M., Böttger, T., Schneider, J., Drewnick, F., Roth, A., Curtius, J., Voigt, C., Borbon, A., Beekmann, M., Bourdon, A., Perrin, T., and Borrmann, S.: Characterization of a Newly Developed Aircraft-Based Laser Ablation Aerosol Mass Spectrometer (ALABAMA) and First Field

Deployment in Urban Pollution Plumes over Paris During MEGAPOLI 2009, Aerosol Science and Technology, 45, 46-64, 2011.

Dall'Osto, M., Beddows, D. C. S., Kinnersley, R. P., Harrison, R. M., Donovan, R. J., and Heal, M. R.: Characterization of individual airborne particles by using aerosol time-of-flight mass spectrometry at Mace Head, Ireland, J. Geophys. Res.-Atmos., 109, D21302, https://doi.org/10.1029/2004JD004747, 2004.

Spencer, M. T., Furutani, H., Oldenburg, S. J., Darlington, T. K., and Prather, K. A.: Gold Nanoparticles as a Matrix for Visible-Wavelength Single-Particle Matrix-Assisted Laser Desorption/Ionization Mass Spectrometry of Small Biomolecules, The Journal of Physical Chemistry C, 112, 4083-4090, 2008.